

1

## 2 **Supplementary Information for**

### 3 **Mean Precipitation Change from a Deepening Troposphere**

4 **Nadir Jeevanjee, David M. Romps**

5 **Nadir Jeevanjee**  
6 **E-mail: [nadirj@princeton.edu](mailto:nadirj@princeton.edu)**

#### 7 **This PDF file includes:**

- 8     Supplementary text
- 9     Figs. S1 to S12
- 10    References for SI reference citations

## Supporting Information Text

### 1. CRM Simulations

**A. Organization.** The spontaneous organization or ‘self-aggregation’ of convection has been much studied recently (see the review by 1). DAM, however, has not been shown to exhibit this behavior; indeed, the simulations of (2) were initialized in an aggregated state precisely because DAM would not spontaneously aggregate. The simulations in this study are no different, as shown in Fig. S1 below, which plots snapshots of column relative humidity (CRH) on the last day of each simulation. CRH here is defined as the water vapor path  $\int \rho_v dz$  (kg/m<sup>2</sup>) divided by its saturation value. No organization is evident, and the low CRH values associated with aggregation (0.3 and below, see Fig. 6 of 3) are not observed here. Note that the absence in DAM of both self-aggregation as a well as a sub-grid turbulence scheme is consonant with the results of (4), who show that entrainment of dry air into cloud updrafts via sub-grid turbulence parameterizations can be critical for aggregation.

**B. LW and SW flux divergence profiles.** The main text argues that  $(-\partial_T F^{\text{LW}})(T)$  and  $(-\partial_T F^{\text{SW}})(T)$  are separately  $T_s$ -invariant. We confirm this in Figs. S2 and S3, which as in Fig. 2 plot  $-\partial_T F$  profiles in  $z$ ,  $p$ , and  $T$  coordinates, but for the LW and SW bands separately.

**C. CRM clear-sky flux divergence profiles.** The argument given in the main text for the  $T_s$ -invariance of  $-\partial_T F$  is a clear-sky argument, but all-sky flux divergences are shown in Figs. 2, S2 and S3. We argue in the main text that this is permissible because cloud fraction in these simulations never surpasses  $\sim 10\%$  at any height, so it is the clear-sky physics which dominates. This claim is supported by the left and center panels of Fig. S4, which shows that the clear-sky flux divergence profiles are almost indistinguishable from the all-sky profiles in Figs. S2 and S3, and are also indeed  $T_s$ -invariant. The right panel of Fig. S4 directly contrasts the all-sky and clear-sky  $-\partial_T F^{\text{net}}$  profiles for the  $T_s = 300$  K simulation, and confirms that the cloud-radiative effect in these simulations is not dramatic.

### 2. Optical depth profiles

The main text argues that water vapor optical depth  $\tau_\lambda(T)$  is  $T_s$ -invariant. This argument was put forth by (5) and (6), but has to our knowledge never been explicitly checked with a comprehensive radiative transfer calculation. Doing so with RRTM is not straightforward, however, as RRTM is a ‘correlated- $k$ ’ model producing band-averaged output, where each band (there are 16 in the LW) covers a wide range of absorption coefficients and optical depths (7). We thus turn to a different, line-by-line radiative transfer model, RFM (8). Feeding average  $p$ ,  $T$ , and specific humidity profiles into RFM with the water vapor continuum turned on and no CO<sub>2</sub> produces the optical depth profiles shown in Fig. S5. These show a reasonable degree of  $T_s$ -invariance across a wide range of surface optical depths (and hence absorption coefficients). Deviations from perfect  $T_s$ -invariance are likely due to pressure broadening as well as changes in lapse rate  $\Gamma(T)$  between simulations, but this requires further investigation. Temperature scaling factors should not contribute to deviations from  $T_s$ -invariance since these are also  $T_s$ -invariant functions of  $T$  (e.g. Eq. (4.62) of reference 9).

### 3. GCM analysis

**A. Variance of  $-\partial_T F^{\text{net}}$  and  $\Gamma(T)$ .** Figure S6 plots the variance  $\text{Var}(\Gamma)$  of  $\Gamma(T)$  within  $T_s$  bins for various  $T_s$  for the IPSL model (other models show similar results). A pickup in variance in the lower atmosphere is evident, and a candidate  $T_{\text{ext}}$  is given by the minimum temperature satisfying  $T > 240$  K (to avoid the large variance regions in the upper atmosphere) and  $\text{Var}(\Gamma) > 0.5$  K<sup>2</sup>/km<sup>2</sup>, plotted in black dots and the dashed lines.

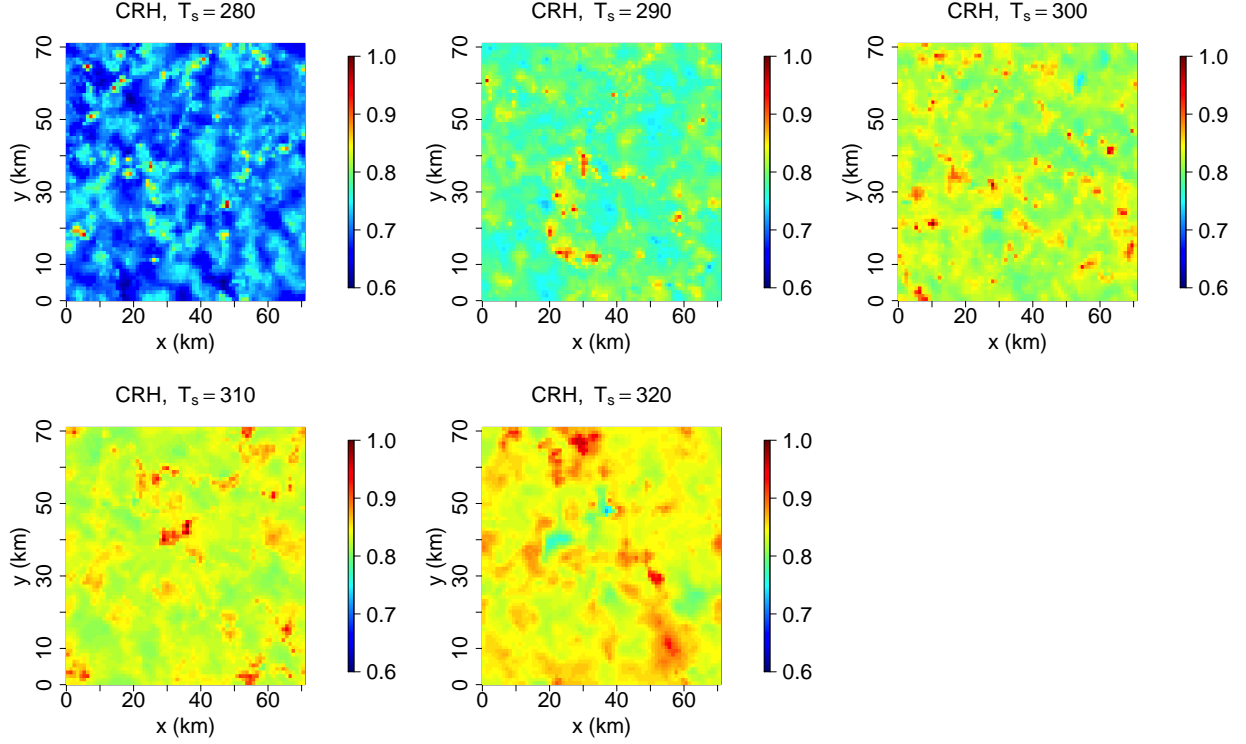
By Eqns. (4–6) of the main text this implies a similar pickup in variance in  $-\partial_T F^{\text{net}}$ , shown in Figure S7 (other models again show similar results, and calculations using clear-sky fluxes show a similar sharp pickup in variance, though the relatively large variances ultimately reached in the surface-based layers are sometimes smaller). We then obtain a second candidate  $T_{\text{ext}}$  as the minimum temperature level satisfying  $T > 240$  K and  $\text{Var}(-\partial_T F^{\text{net}}) > 5$  (W/m<sup>2</sup>/K)<sup>2</sup>. This  $T_{\text{ext}}$  is again shown by black dots and dashed lines, and values are reasonably close to those obtained from  $\text{Var}(\Gamma)$ . If the  $T_{\text{ext}}$  candidate derived from  $\text{Var}(-\partial_T F^{\text{net}})$  exists then it is used for  $T_{\text{ext}}$ , as it better represents where the AMIP and AMIP4K  $-\partial_T F^{\text{net}}$  profiles diverge; if this  $T_{\text{ext}}$  candidate does not exist (as for the  $T_s=250$  K bin of the IPSL model), then  $T_{\text{ext}}$  as diagnosed from  $\text{Var}(\Gamma)$  is used.

**B. AMIP<sub>ext</sub> profiles for other  $T_s$  bins.** Figure 6 suggests that AMIP<sub>ext</sub> profiles are often a good approximation to the AMIP4K profiles, but this is not always the case (e.g. the IPSL panel). For a better sense of the robustness of agreement between AMIP<sub>ext</sub> and AMIP4K profiles, we show the analogous panels but for the  $T_s=280$  K bins, rather than  $T_s = 290$  K, in Fig. S8. These show that AMIP<sub>ext</sub> profiles are typically a good approximation to the AMIP4K profiles, and that a failure of these profiles to line up seems to be the exception rather than the rule.

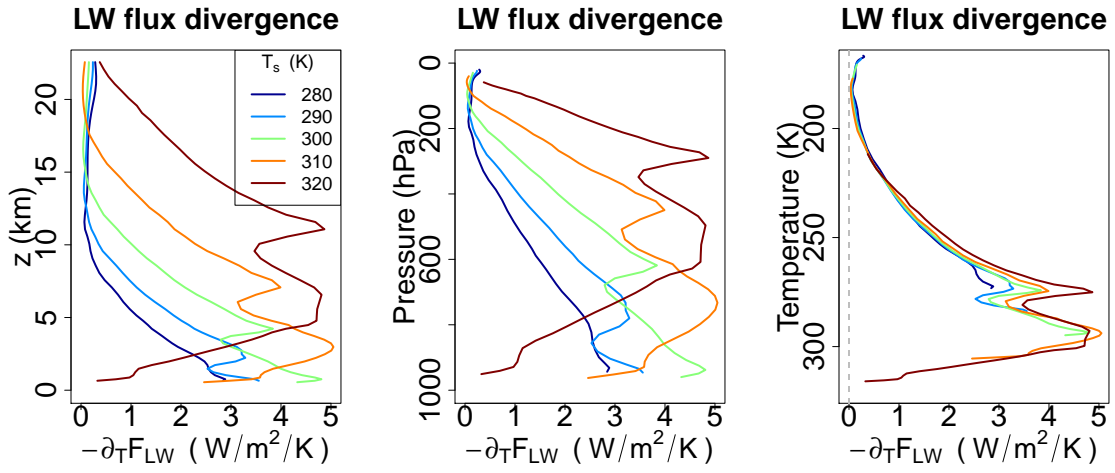
**C. GCM clear-sky flux divergence and relative humidity profiles.** In the main text we claimed that the near-surface features in the GCM  $-\partial_T F^{\text{net}}$  profiles in Figs. 5 and 6 were sometimes, but not always, due to cloud radiative effects (CRE). Figure S9 show both all-sky and clear-sky  $-\partial_T F^{\text{net}}$  profiles for the AMIP case for all models for the  $T_s = 270$  K bin, for which many models show a significant near-surface CRE. Figure S10, which is analogous to Fig. S9 but for the  $T_s = 290$  K bin, shows on the other hand that in this  $T_s$  bin the near-surface CRE across models is less consistent and less significant.

Figure S11 supports the claim in the main text that  $T_s$ -binned RH profiles also exhibit  $T_s$ -invariance aloft, but have near-surface features which shift downwards with warming. RH profiles are binned exactly as for the radiative fluxes, as described in *Materials and Methods*.

Figure S12 shows all-sky  $-\partial_T F^{\text{LW}}$  and  $-\partial_T F^{\text{SW}}$  for the  $T_s=290$  K (AMIP) and  $T_s=294$  K (AMIP4K) bins for all our CFMIP models, demonstrating that the  $T_s$ -invariance in GCMs holds for both the LW and SW separately, just as for the CRM (Figs. S2 and S3).



**Fig. S1.** Snapshots of column relative humidity (CRH) from the last day of each RCE simulation. No organization is evident, and the low CRH values associated with aggregation ( $\lesssim 0.3$ ) are not observed.



**Fig. S2.** LW flux divergence  $-\partial_T F^{\text{LW}}$ , as diagnosed from RRTM coupled to our CRM RCE simulations at  $T_s=(280, 290, 300, 310, 320)$  K. Fluxes are plotted from the lifting condensation level of each simulation to 22.5 km for clarity, and in height, pressure, and temperature coordinates to emphasize the  $T_s$ -invariance of  $(-\partial_T F^{\text{LW}})(T)$ .

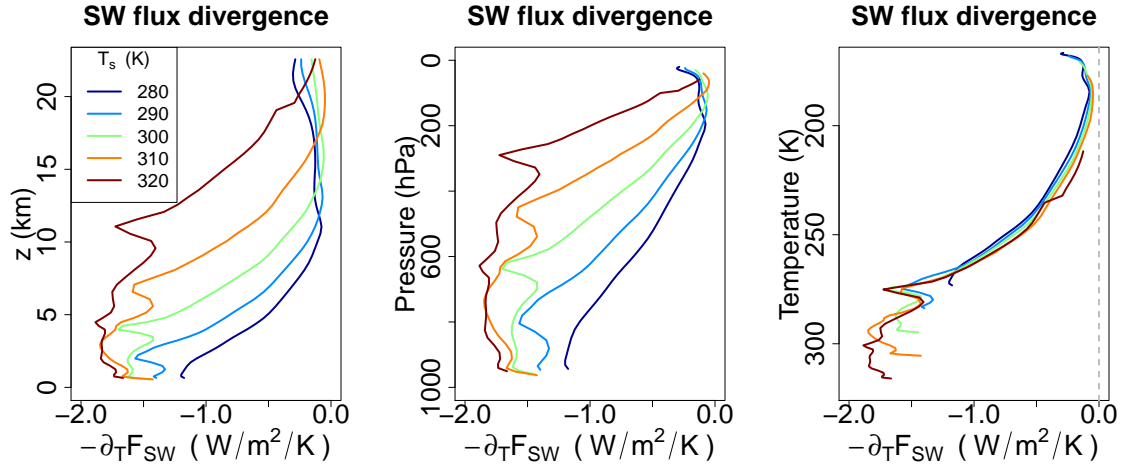


**Fig. S3.** As in Fig. S2, but for the SW band.

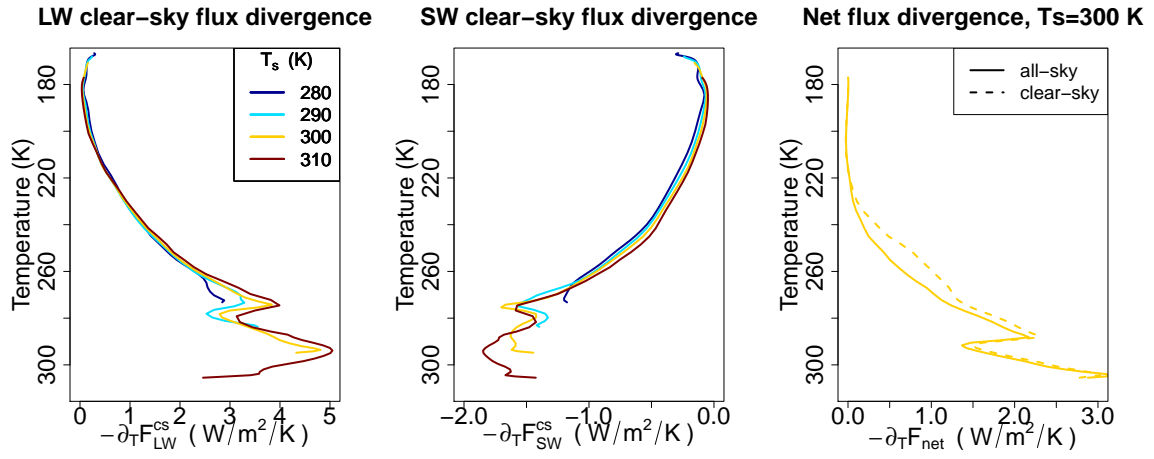


**Fig. S4.** Left: Clear-sky LW flux divergence  $-\partial_T F_{\text{cs}}^{\text{LW}}$  Center: Clear-sky SW flux divergence  $-\partial_T F_{\text{cs}}^{\text{SW}}$  Right: Clear-sky and all-sky net flux divergence for the  $T_s = 300$  K simulations, all plotted as in Fig. 2. The left and center panels are almost identical to the right panels of Figs. S2 and S3, and the right panel above shows directly the small difference between the all-sky and clear-sky flux divergences for the  $T_s=300$  K simulation.

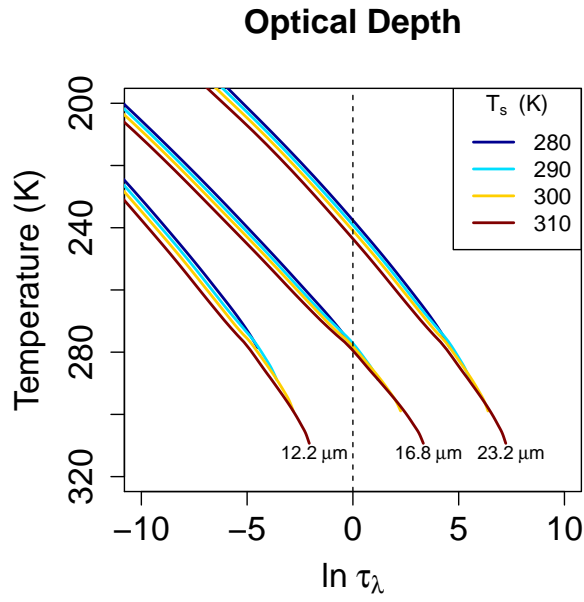


**Fig. S5.** Optical depth profiles  $\tau_\lambda(T)$ , obtained by feeding thermodynamic profiles from the RCE simulations into the RFM line-by-line radiative transfer code. Profiles are shown for water vapor only at three different wavelengths corresponding to surface optical depths of 0.01, 1, and 100 in the  $T_s=280$  K simulation. A reasonable degree of  $T_s$ -invariance is seen at each wavelength: over the 30 K range of  $T_s$ , the temperature at which these lines reach  $\tau_\lambda = 1$  for example (where cooling-to-space is maximized) varies by at most 8 K, or a little over 25% of the  $T_s$  range.

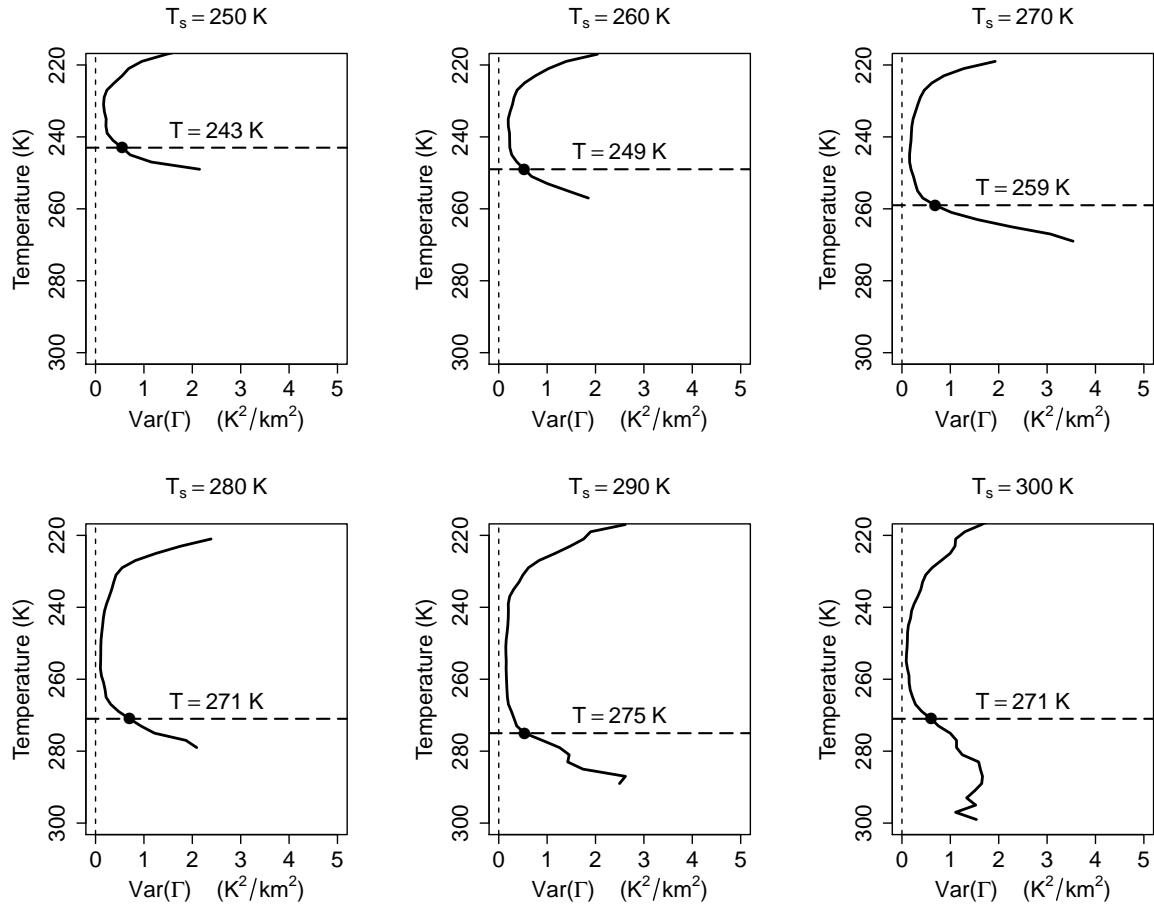


**Fig. S6.** Variance of  $\Gamma(T)$  within  $T_s$  bins for the IPSL model. A fairly sharp pickup in the lower atmosphere is evident, similar to that found for  $-\partial_T F^{\text{net}}$  profiles (Fig. S7). Black dots and dashed lines mark where the profiles exceed a threshold of  $0.5 \text{ K}^2/\text{km}^2$  in the lower troposphere, showing that  $T$  where the variance in  $\Gamma$  picks up is comparable to the  $T_{\text{ext}}$  diagnosed from the variance in  $-\partial_T F^{\text{net}}$ .



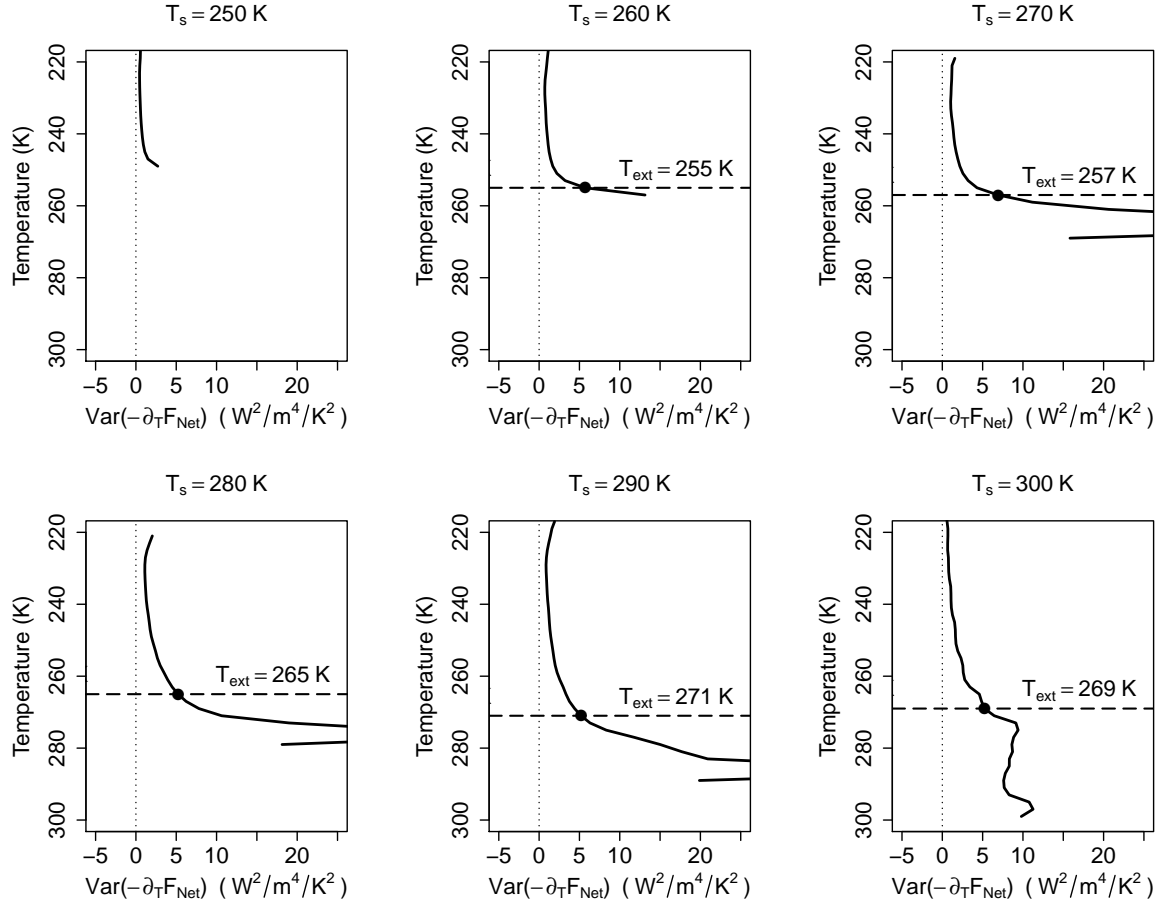


**Fig. S7.** Variance of  $-\partial_T F^{\text{net}}$  within  $T_s$  bins for the IPSL model. A fairly sharp pickup in the lower atmosphere is evident for most bins, which is then used to diagnose  $T_{\text{ext}}$ , plotted in black dots. See SI text 3A for details.

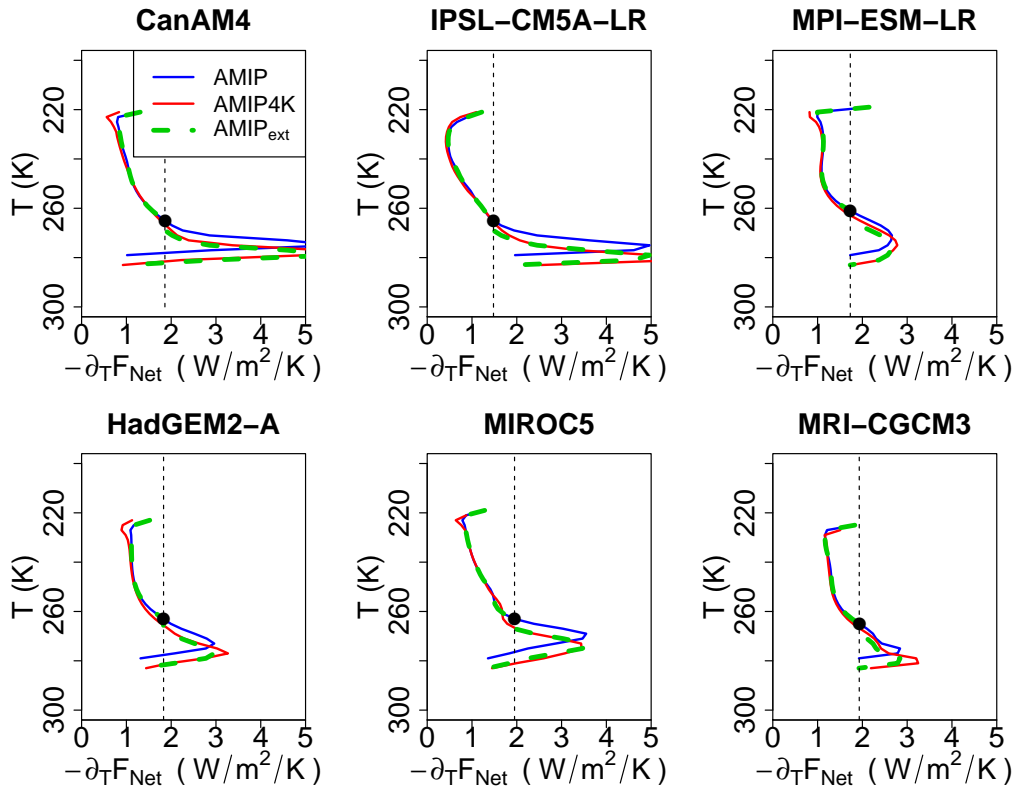


**Fig. S8.** As in Fig. 6 of the main text but for the  $T_s = 280$  K bins.

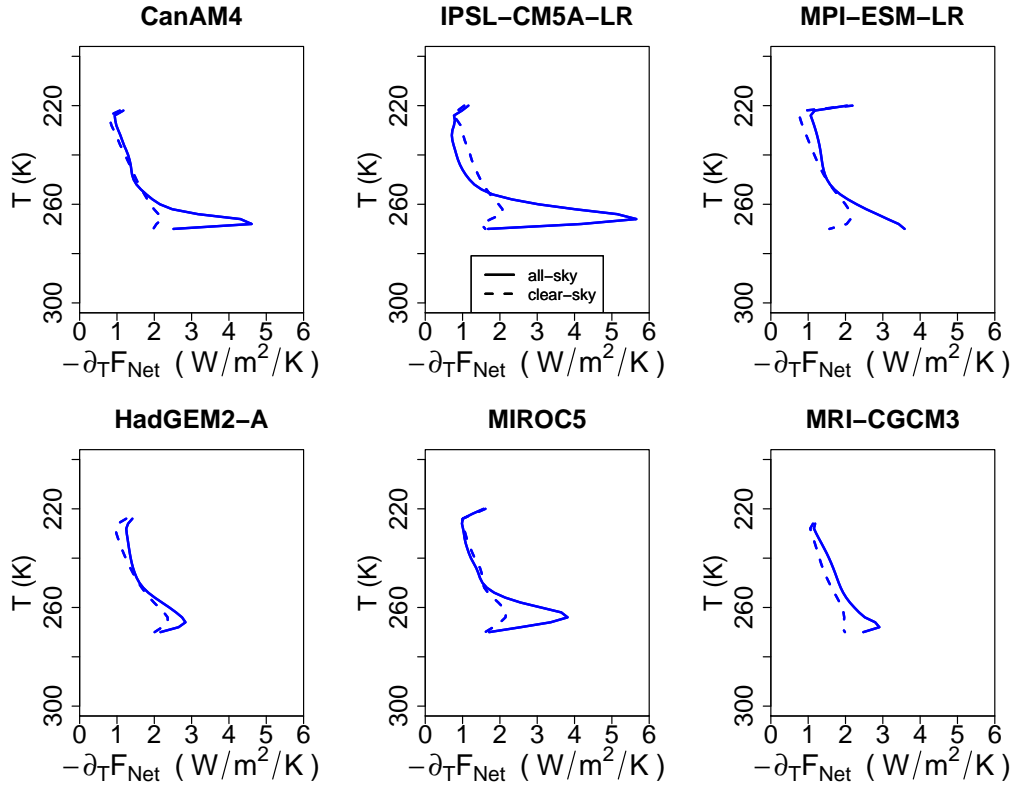


**Fig. S9.** All-sky and clear-sky  $-\partial_T F^{\text{net}}$  profiles for the AMIP case for all models for the  $T_s = 270$  K bin. The majority of models show a significant near-surface CRE.

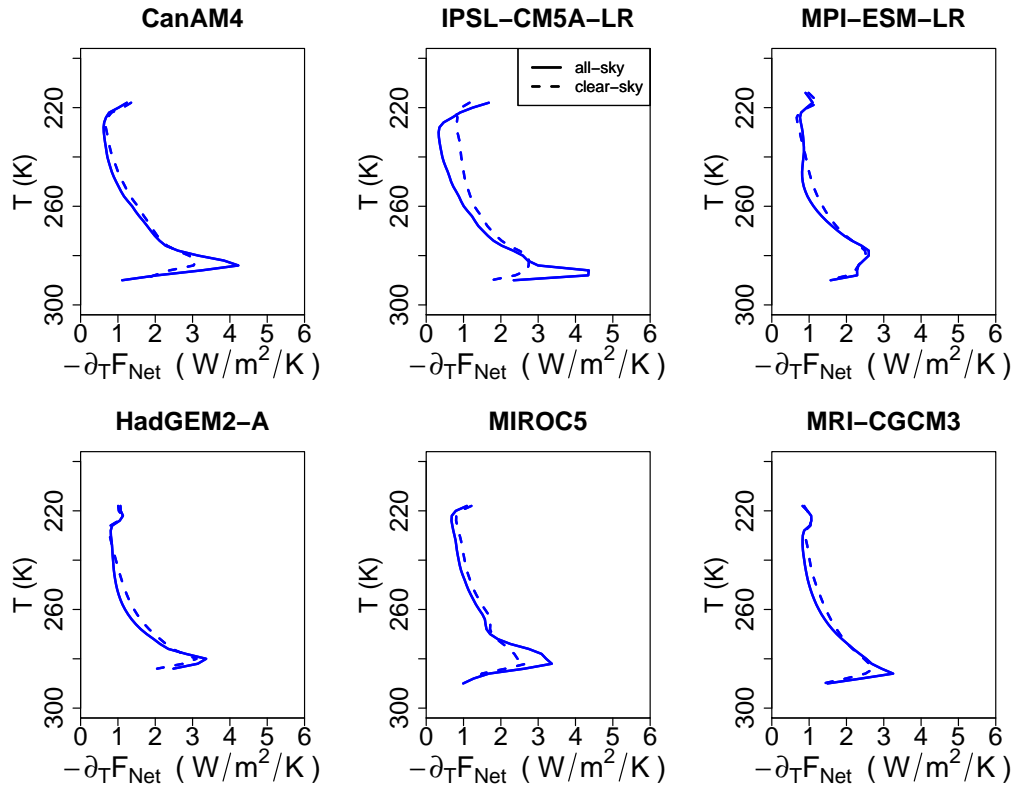


**Fig. S10.** As in Fig. S9, but for the  $T_s = 290$  K bin. The near-surface CRE is much less significant across models than for the  $T_s = 270$  K bin.

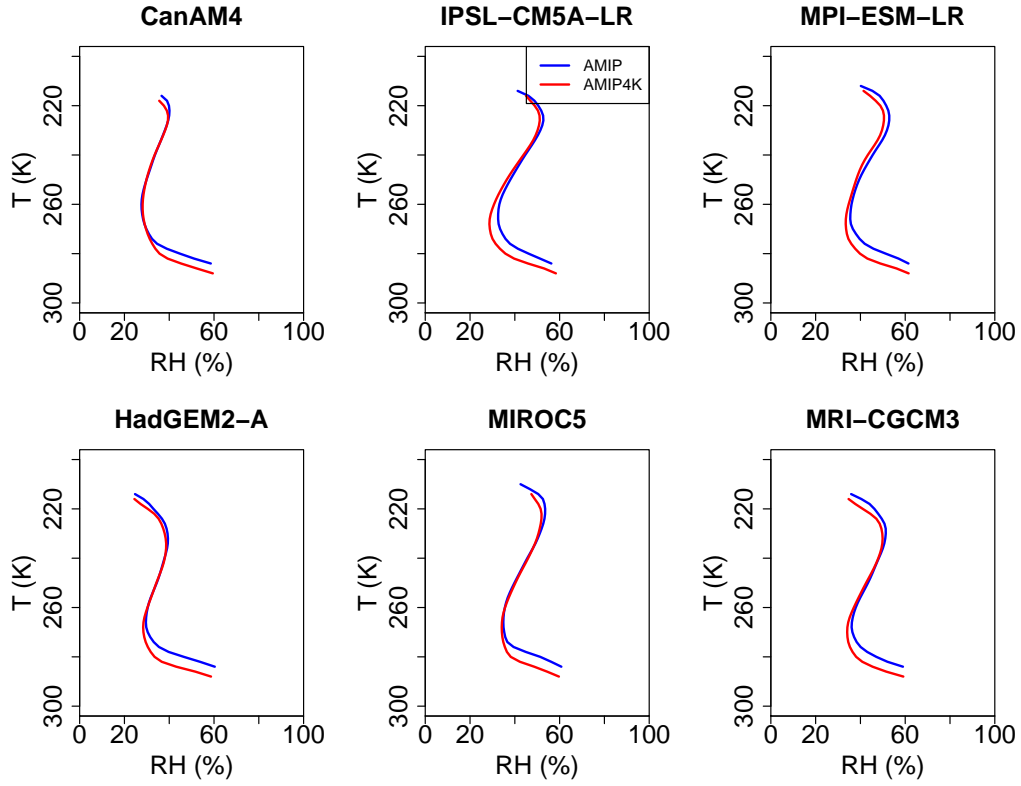


**Fig. S11.** RH profiles for our CFMIP models for the  $T_s = 290$  (AMIP) and  $T_s = 294$  K (AMIP4K) bins, computed just as for radiative fluxes. Like the  $-\partial_T F^{\text{net}}$  profiles, the RH profiles show  $T_s$ -invariance aloft, but have lower-tropospheric features which shift downward (in temperature space) with warming.

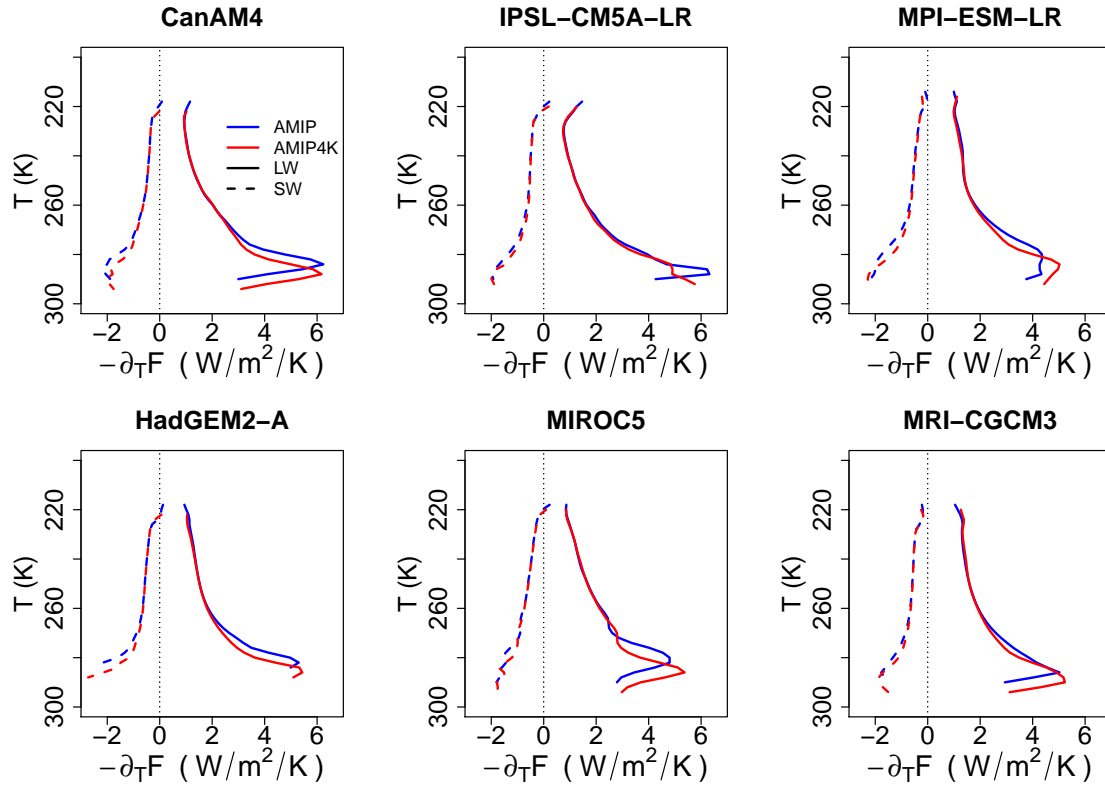


**Fig. S12.** Profiles of  $-\partial_T F^{SW}$  and  $-\partial_T F^{LW}$  for the  $T_s=290$  K (AMIP) and 294 K (AMIP4K) bins for all six CFMIP models. This is similar to Fig. 6 of the main text, but with the flux divergence decomposed into the LW and SW bands to show that  $T_s$ -invariance in the mid and upper troposphere holds across models holds for both the LW and SW separately, just as for the CRM.

## 70 References

- 71 1. Wing AA, Emanuel K, Holloway CE, Muller C (2017) Convective Self-Aggregation in Numerical Simulations: A Review.
- 72 2. Jeevanjee N, Romps DM (2013) Convective self-aggregation, cold pools, and domain size. *Geophysical Research Letters*
- 73 40(5):994–998.
- 74 3. Bretherton CS, Blossey PN, Khairoutdinov MF (2005) An Energy-Balance Analysis of Deep Convective Self-Aggregation
- 75 above Uniform SST. *Journal of the Atmospheric Sciences* 62(12):4273–4292.
- 76 4. Tompkins AM, Semie (2017) Organization of tropical convection in low vertical wind shears: Role of updraft entrainment.
- 77 *Journal of Advances in Modeling Earth Systems* 6:513–526.
- 78 5. Simpson G (1928) Some Studies in Terrestrial Radiation. *Memoirs of the Royal Meteorological Society* 2(16):69–95.
- 79 6. Ingram WJ (2010) A very simple model for the water vapour feedback on climate change. *Quarterly Journal of the Royal*
- 80 *Meteorological Society* 136(646):30–40.
- 81 7. Mlawer EJ, Taubman SJ, Brown PD, Iacono MJ, Clough SA (1997) Radiative transfer for inhomogeneous atmospheres:
- 82 RRTM, a validated correlated-k model for the longwave. *Journal of Geophysical Research* 102(D14):16663.
- 83 8. Dudhia A (2017) The Reference Forward Model (RFM). *Journal of Quantitative Spectroscopy and Radiative Transfer*
- 84 186:243–253.
- 85 9. Pierrehumbert RT (2010) *Principles of Planetary Climate*. (Cambridge University Press).